Journal of Materials Chemistry B

Influence of Chemical Heterogeneity and Microstructure on the Corrosion Resistance of Biodegradable WE43 Magnesium Alloys

Journal:	*Journal of Materials Chemistry B*
Manuscript ID	TB-ART-02-2019-000388.R2
Article Type:	Paper
Date Submitted by the Author:	09-May-2019
Complete List of Authors:	Mraied, Hesham; University of South Florida Wang, Wenbo; Virginia Polytechnic Institute and State University Cai, Wenjun; Virginia Polytechnic Institute and State University

Influence of Chemical Heterogeneity and Microstructure on the Corrosion Resistance of Biodegradable WE43 Magnesium Alloys

Hesham Mraied[1], Wenbo Wang[2], and Wenjun Cai[2,*]

1. Department of Civil and Environmental Engineering, University of South Florida, 4202 E Fowler Avenue, Tampa, FL 33620, USA
2. Department of Materials Science and Engineering, Virginia Polytechnic Institute and State University, Blacksburg, VA 24060, USA

Abstract

Magnesium-yttrium-rare earth elements alloys such as WE43 are potential candidates for future bioabsorbable orthopedic implant materials due to their biocompatibility, mechanical properties similar to human bone, and the ability to completely degrade in vivo. Unfortunately, the high corrosion rate of WE43 Mg alloys in physiological environments and subsequent loss of structural integrity limit the wide applications of these materials. In this study, the effect of chemical heterogeneity and microstructure on the corrosion resistance of two alloys with different metallurgical states were investigated: cast (as in traditional preparation) and as-deposited produced by magnetron sputtering. The corrosion behavior was studied by potentiodynamic polarization and electrochemical impedance spectroscopy tests in blood bank buffered saline solution. It was found that the as-deposited alloy showed more than one order of magnitude reduction in corrosion current density compared to the cast alloy, owing to the elimination of micro-galvanic coupling between the Mg matrix and the precipitates. The microstructure and formation mechanism of corrosion products formed on both alloys were discussed based on immersion tests and direct measurements of X-ray photoelectron spectrometry (XPS) and cross-sectional transmission electron microscopy (TEM) analysis.

Keywords: Magnesium alloy; microstructure; corrosion; EIS; TEM; XPS

* Email: caiw@vt.edu

1. Introduction

Biodegradable WE43 Mg alloy with major alloying elements of yttrium (Y, 4.1 wt%), neodymium (Nd, 2.1 wt%), and zirconium (Zr, 0.56 wt%) has received much interest lately for potential applications as temporary cardiovascular stents [1, 2] and bone implants [3, 4]. Mg alloys exhibit good cell adhesion in physiological environment and can safely degrade in the human body; hence no post operation is required once the damaged tissue is healed, minimizing procedure cost and risks [5, 6]. In contrast to conventional medical metallic materials such as titanium, cobalt-chromium, and stainless steel, the mechanical properties of Mg are close to that of human bones [7, 8], thus minimizing the stress shield effect [9] and increasing implant stability [7]. Moreover, Mg is an essential element for human metabolic processes and has been shown to enhance bone growth when used as implants [10-12].

Unfortunately, the high degradation rate of Mg alloys in physiological environments [13, 14] and subsequent loss of structural integrity and extensive hydrogen evolution to balance the anodic dissolution [15, 16], limit their wide application. When tested in vivo, Witte et al. [17] found that WE43 Mg alloy completely degraded within 18 weeks. Corrosion of Mg occurs mainly per the half-cell reactions shown in equations 1 and 2. The electrons released by the anodic reaction are consumed by the cathodic reaction to generate H_2 gas [18]. The Mg^{2+} and OH^- ions formed by the anodic and cathodic reactions, respectively, will then combine to form a $Mg(OH)_2$ film according to equation 3 [19, 20];

$$Mg \rightarrow Mg^{2+} + 2e^- \text{ (anodic)}, \quad (1)$$

$$2H_2O + 2e^- \rightarrow H_2 + 2OH^- \text{ (cathodic)}, \quad (2)$$

$$Mg^{2+} + 2OH^- \rightarrow Mg(OH)_2. \quad (3)$$

The selection of proper alloying elements with specific composition is a common approach to enhance the mechanical properties and corrosion resistance of Mg [21], as reflected in the composition of WE43 Mg alloy. The addition of Y promotes precipitation strengthening [21, 22], In combination with other rare earth elements Y also enhances the creep resistance [21]. Nd was found to be biocompatible [23, 24] and effective in enhancing the corrosion resistance of Mg alloys by reducing micro-galvanic effects due

to the presence of intermetallic compounds [25-27]. Nd also enhances the mechanical properties of Mg by forming intermetallic phases at the grain boundaries [25, 28, 29]. Zr addition increases the strength of Mg mainly by grain refinement [12]. Due to the limited solubility of Zr in Mg, the undissolved Zr particles act as selective nucleation cites during solidification. The corrosion resistance of Mg was found to be enhanced when the concentration of Zr is kept below 2% [21].

While alloying is a convenient method to enhance the mechanical properties of Mg, its effect on corrosion resistance is often complicated and detrimental. For example, most Mg alloys exhibits corrosion rate much higher than that of high purity Mg [30]. This is because the formation of precipitates and secondary phases often leads to undesired micro-galvanic coupling between the precipitates and α-Mg matrix, considered to be a dominating corrosion mechanism of Mg alloys. For precipitate-containing Mg alloys, corrosion of the Mg matrix often dominates the overall corrosion behavior of the alloy. Since most (although not all [31]) precipitates are nobler than the Mg matrix, the latter normally serves as micro-anode and the precipitates as cathodes. Thus the size and distribution of precipitates might affect the precipitate-matrix galvanic coupling and hence control the corrosion rate. In this work, to evaluate the roles of precipitates on the corrosion rate of WE43, corrosion study was performed on WE43 of two metallurgical states: cast and as-deposited. The commercially produced cast samples contain extensive precipitates due to limited solubility of alloying elements in Mg, hence representing a microstructure with high level of chemical heterogeneity. The deposited samples, prepared using a non-equilibrium processing technique (i.e. physical vapor deposition), contain supersaturated solid solution of all elements, hence representing a microstructure nearly without chemical heterogeneity. Corrosion testing, in-situ image monitoring, and post-corrosion microstructure characterization were combined to determine the roles of chemical heterogeneity and microstructure on the corrosion mechanism of the alloy in a simulated physiological environment.

2. Materials and methods

2.1. Materials synthesis

Cast WE43 Mg sheets (1 mm thickness) and sputtering targets with the same global composition of 4.1 wt.% Y, 2.1 wt.% Nd, 0.56 wt.% Zr, and balance Mg, were obtained from AEM Products. The cast sheets were cut into several 25x15 mm^2 rectangles for the electrochemical tests. Prior to corrosion testing, the cast samples were mechanically polished using a series of SiC abrasive papers down to 2400 grit size, followed by 0.3 μm alumina polish suspension (Pace Technologies), rinsed with di-water, and air dried. The thin film samples were prepared by DC magnetron sputtering (CRC-100 sputter coater) on (100) Si wafers. Prior to sputtering, the Si wafers were chemically etched using hydrofluoric acid to remove the native oxide film. Sputtering was conducted inside a vacuum chamber (5 mTorr working pressure) with argon atmosphere at 100 μA current for 3hr hours to achieve a nominal film thickness of ~ 570 nm.

2.2. Microstructure characterization

The microstructure of cast and as-deposited (hereafter referred as CT- and AD-WE43) samples, was studied by grazing incidence x-ray diffraction (GIXRD, X'Pert PANalytical), using Cu Kα (1.5404 Å) radiation at 40 kV and 40 mA. Data was collected over 2θ values of 20-80°, 0.015° step size, and 3.5 s per step. The diffraction patterns were then analyzed using X'Pert Highscore software. The surface morphology and composition were characterized using scanning electron microscopy (SEM, Hitachi SU-70) and calibrated energy-dispersive X-ray spectroscopy (EDS, EDAX-Phoenix). EDS analysis was carried out using acceleration voltage of 10 kV. Transmission electron microscopy (TEM) analysis of AD-WE43 samples, including bright-field (BF), dark-field (DF) imaging, and selected area diffraction (SAD) were performed using a (Tecani F20) TEM operated at 200 kV. Plane view TEM samples of AD-WE43 samples were prepared by directly sputtering the alloy on continuous carbon film TEM grids for 15 min, which resulted in a sample thickness of ~150 nm. Cross-sectional TEM samples of AD-WE43 samples were prepared by focused ion beam microscope (FIB, Quanta 200 3D Dual Beam) on as-deposited AD-WE43 sample using standard lift-out methods. Prior to the lift-out, a carbon protective layer (~ 500 nm) was e-beam deposited, followed by an ion-beam deposited Pt layer (~ 1-2 micron).

2.3. Electrochemical tests

An effective area of 1 cm² of all samples was obtained by using a Gamry PortHole™ electrochemical sample mask for the electrochemical tests. All electrochemical measurements were performed at room temperature (21 ± 2 °C) using a Gamry Reference 600® potentiostat with the conventional three electrode configuration in naturally aerated and stagnant blood bank buffered saline (BBBS) having a pH of 7.0-7.2 and composition in g/L NaCl: 8.5, Na_2HPO_4: 1.67 and Na_2HPO_4: 0.39. The sample, mixed metal oxide coated titanium mesh, and a commercial silver-silver chloride electrode (1 M KCl internal solution) were used as the working, counter, and reference electrodes, respectively.

Potentiodynamic polarization (PD) measurements were conducted in a single upward scan at a constant scan rate of 1 mV/s, starting from a cathodic potential (~ 150 mV below the open circuit potential E_{OC}) to an anodic potential (~ 300 mV above E_{OC}). Electrochemical impedance spectroscopy (EIS) tests of all samples were conducted after 15 min of immersion in the electrolyte at E_{OC} in the frequency range of 100 kHz to 100 mHz, 5 points per decade, and 10 mV rms sinusoidal potential excitation. The EIS data were then fitted using Gamry E-chem software. The evolution of H_2 gas during immersion test was measured for both samples during an exposure period of 24 hrs using an experimental setup shown in Figure 7(a). The BBBS volume to specimen's surface area ratio of 30 ml/cm^2 was used for both samples and the immersion solution was renewed every 8 hr to avoid the pH increase due to hydroxides formation [32, 33]. All exposures were conducted at room temperature. All results reported hereafter correspond to the average from at least three separate samples at each test condition. Variability is reported here and for the other observations in this paper as the range of the replicate test results.

2.4. Corrosion products characterization

The post corrosion surface and cross-sections of samples were characterized using scanning electron microscopy (SEM, Hitachi SU-70) and calibrated energy-dispersive X-ray spectroscopy (EDS, EDAX-Phoenix). The cross-sectional samples were prepared by focused ion beam microscope (FIB, Quanta 200 3D Dual Beam) operated at 20 kV using Ga ions. The chemical state analysis of corroded samples was conducted by

x-ray photoelectron spectroscopy (XPS, Perkin Elmer 5100) using Al Kα radiation source at constant pass energy of 89.45 eV, step size of 0.5 eV and 10 total sweeps. Transmission electron microscopy (TEM) analysis and EDS line scans were performed on sample cross-sections after electrochemical tests, using a Tecani F20 TEM operated at 200 kV. The TEM samples were prepared by FIB using standard lift-out methods. Prior to the lift-out, a carbon protective layer (~ 500 nm) was e-beam deposited, followed by an ion-beam deposited Pt layer (~ 1-2 micron), on the sample surface to protect the outermost (corroded) surface from ion beam damages during FIB.

3. Results and discussion

3.1. Microstructure characterization

Figure 1 (a) shows the surface morphology and the corresponding EDS element maps of CT-WE43. The microstructure consists of a solid solution of α-Mg matrix and randomly distributed intermetallic precipitates with high Y, Nd, and Zr content [34], which were formed during solidification. These precipitates have three different shapes; longitudinal, cuboidal, and spherical, as indicated in Figure 1(a). The average length of the longitudinal precipitates is 22.0 ± 3.0 μm, while the average size of the cuboidal and the spherical particles is 3.5 ± 0.5 and 6.0 ± 0.7 μm, respectively. EDS element maps in Figure 1(a) show that the longitudinal and spherical precipitates are rich in Nd while the cuboidal particles are rich in both Y and Zr. Table 1 summarizes the compositions of these precipitates. It can be seen that the longitudinal and spherical phases have higher Nd concentration, while the cuboidal phase showed enriched Y and Zr concentration. These findings agree with those of Liu et al.[35], who found that the longitudinal, cuboidal, and spherical phases are enriched in Nd, Y, and Zr, respectively.

The surface morphology of the AD-WE43 (Figure 1(b)) exhibited dense faceted angular structures, which are often associated with the formation of a nanocrystalline phase having columnar through thickness grains [36]. The EDS analysis in Table 1 suggested that the global composition of AD-WE43 is very close to that of CT-WE43. The corresponding EDS element maps in Figure 1(b) indicated that all alloying elements are homogeneously distributed within the α-Mg matrix, without detectable precipitation at the EDS resolution limit (~ 200 nm).

Figure 2 shows the XRD results of both alloys. In CT-WE43, phases correspond to α-Mg as well as $Mg_{41}Nd_5$ and $Mg_{24}Y_5$ precipitates were observed. While the current XRD data base does not include results from $Mg_{24}(Y, Zr)_5$ phases, it is likely that the XRD identified $Mg_{24}Y_5$ phase also contains Zr, as indicated by prior EDS results (Figure 1 and Table 1), also reported before [37]. On the other hand, only α-Mg phase was observed in AD-WE43, indicating the supersaturation of Y, Zr, and Nd in the α-Mg matrix [38, 39]. It is also noted that the AD-WE43 exhibited a strong $(11\bar{2}0)$ fiber texture in the film thickness direction, similar to those reported in other PVD deposited Mg alloys [40]. To further characterize the microstructure of the AD-WE43, TEM analysis was performed on both plane-view and cross-sectional samples, as shown in Figure 3. It can be seen that columnar through thickness grains were observed, with an average in-plane grain size of 46.6 ± 12.4 nm, measured using line-intercept method from multiple DF images. The SAD pattern (Figure 3(b) inset) exhibited diffraction rings of a single hcp phase, in agreement with the XRD results.

3.2. Potentiodynamic polarization study

Figure 4 shows representative PD results of both alloys after immersion in BBBS for 20 min. The anodic and cathodic branches of the PD curve are assumed to represent the anodic dissolution of Mg and cathodic hydrogen evolution, respectively. Both alloys showed significant corrosion activity, as is common with Mg alloys [41]. However, it can be seen that AD-WE43 exhibited a shift of both anodic and cathodic branches towards lower corrosion current densities (i_{cor}), with only moderate change in the crossover potentials for zero current (E_{zc} , which was close, as expected, to E_{OC}). This pattern indicated a decrease in both anodic and cathodic kinetics of the AD-WE43 compared with those of the CT-WE43 [20, 42]. This relative trend was clearly reproduced on triplicate testing as illustrated in the inset of Figure 4. In addition, the anodic branch of CT-WE43 showed very little polarizability, indicative of a strongly active dissolution. In contrast, the anodic branch of AD-WE43 showed comparatively modest polarization up to about -1.4 $V_{Ag/AgCl}$, suggesting the presence of a somewhat protective film on the alloy surface that breaks down above that potential [8, 43].

Table 2 lists E_{OC} and the electrochemical parameters obtained from PD tests. The average values of E_{OC} of both alloys were about -1.5 $V_{Ag/AgCl}$. These values were comparable to those reported elsewhere for cast WE43 Mg alloy tested at 37 ^{o}C in NaCl aqueous solutions (-1.9 to -1.8 $V_{Ag/AgCl}$), simulated body fluids (SBF) (-1.9 to -1.6 $V_{Ag/AgCl}$) and complete cell culture medium (-1.7 to -1.6 $V_{Ag/AgCl}$) [3, 8, 9, 44, 45]. Due to the asymmetry of the anodic and cathodic branches of the PD curves, in this work nominal values of i_{cor} were estimated by Tafel extrapolation of only the cathodic region, using data from potentials that were more than 50 mV more negative than $E_{OC.}$[44, 46]. As shown in Figure 4 and Table 2, AD-WE43 exhibited a strong (more than one order of magnitude) reduction in the corrosion current density (μA/cm²), compared to that of the CT-WE43. Additional tests (not shown here) of CT-WE43, which included a return scan at an apex potential of -300 mV vs. E_{OC} showed a return loop, indicating the susceptibility of the alloy to localized corrosion. In contrast, those from AD-WE43 revealed no significant hysteresis between the forward and reverse curves. That observation suggested that the chosen scan rate of 1 mV/s during PD tests was appropriate for representing the cathodic kinetics used for i_{corr} estimates. It is interesting to note that the i_{corr} values of as-deposited alloy reported here is as well remarkably lower than that reported for plasma ion implanted WE43 Mg alloy in SBF solution [8, 44, 47].

3.3. Electrochemical impedance spectroscopy study

To further evaluate the corrosion mechanisms of both alloys, EIS measurements were conducted after E_{OC} stabilization for 15 min in BBBS. Short exposure periods were used on account of the relatively rapid rates of the cast alloy wastage, which might have prevented useful comparison with the deposited alloy at later ages. The Nyquist diagram for representative results is shown in Figure 5. The diagrams of both alloys were generally similar in having a single capacitive loop shape, comparable with what could be expected from a polarization resistance resulting from Faradaic processes, coupled with an interfacial charge storage process. Secondary differences, such as a minor inductive component at low frequencies for the cast alloy may be dismissed as possible artifacts from fast interface evolution during the EIS test run. The experimental data were interpreted using the analog equivalent circuit model shown as inset in Figure 5. A

constant phase element (CPE) was used instead of a capacitor due to the depression of the Nyquist curve at low frequencies. R_s represents the ohmic solution resistance. In the simplest form, the solution/metal interface includes a polarization resistance (R_P) and a CPE. The Nyquist results showed that both alloy exhibited similar corrosion mechanism, but the significantly larger capacitive loop of the as-deposited alloy compared to that of the cast alloy indicated an enhanced corrosion resistance[3, 44] that might be achieved by reducing the chemical heterogeneity.

The impedance of the non-ideal capacitance CPE is represented as:

$$Z_{CPE} = Y_o^{-1}(j\omega)^{-n}, \quad (4)$$

where Y_o is a constant, $j = (-1)^{1/2}$, ω is the angular frequency and n is a real number between 0 and 1. As shown in Figure 5, the fitted results closely matched the experimental behavior for much of the frequency range for both alloys. It was found that R_P for the AD-WE43 is 3,700 ± 750 $\Omega.cm^2$, significantly larger than that of the cast alloy (250 ± 90 $\Omega.cm^2$), indicating that the former exhibited reduction in the electrochemical reactions occurring at the metal surface, hence enhancing the resistance to Mg dissolution.

The corrosion current density (i_{corr}) from EIS tests was estimated from the R_P using Stern-Geary equation: [41, 48]

$$i_{corr} = B/R_P. \quad (5)$$

B is the apparent Stern-Geary coefficient and can be estimated from:

$$B = \frac{\beta_a.\beta_c}{2.3(\beta_a + \beta_c)}, \quad (6)$$

where β_a and β_c are the anodic and cathodic Tafel slopes, respectively. It is also noted here, that the validity of corrosion current densities estimated from Stern-Geary equation depends on the correct determination of the coefficient B and whether Mg dissolves directly to Mg^{2+} or through Mg^+ intermediate [41, 49, 50]. In this work the value of B was chosen to be equal to 0.026 V, representing the condition of an active metal. As listed in Table 2, the corrosion current density (μA/cm²) of the AD-WE43 is much lower (less than 10 times) than that of CT-WE43, in good agreement with the PD tests.

3.4. Immersion test

Results in Section 3.2-3.3 showed that eliminating precipitates in AD-WE43 led to more than one order of magnitude reduction in corrosion current density compared to CT-WE43. To understand the differences in anodic and cathodic reaction kinetics during corrosion of both alloys, E_{oc} and hydrogen (H_2) bubble evolution during immersion test are presented in Figures 6 and 7. Figure 6 shows the evolution of E_{oc} for both alloys (test was repeated for at least two samples) during immersion tests up to 15 min. It can be seen that for AD-WE43, E_{oc} increased from ~ −1.67 V vs. Ag/AgCl to ~ −1.52 V vs. Ag/AgCl in the first ~ 180 sec. Such fast increase in E_{oc} is often associated with passivation of the surface and formation of a protective and continuous surface film [51]. In the same experiments, a cotton-tipped thin rod (Q-tip) was used to frequently scrub the sample surface so as to introduce a local disturbance. Such disturbance had negligible effect on E_{oc} of CT-WE43. Interestingly, for AD-WE43, such disturbance led to a sudden decrease in E_{oc}, followed by a gradual recovery once scrubbing stopped. This behavior is characteristic of a typical depassivation-repassivation behavior upon sufficient disturbance or break down of a passive film [52]. Thus the presence of a somewhat protective surface layer is believed to act as a passive film and lower the anodic reaction kinetics of AD-WE43. This surface layer may consist of loosely adhering corrosion product. Upon disturbance with a soft Q-tip, such oxide layer may be fragmented and become temporarily non-protective. The relatively fast repassivation that follows quickly afterward is possibly due to an associated pH rise in the surface area [53]. Figure 7 shows the hydrogen evolution of both samples up to 24 hrs. During the entire immersion period, AD-WE43 developed less amount of H_2 bubbles and sites of corrosion compared to the cast alloy, indicating a decrease in cathodic kinetics of the AD-WE43, in agreement with the PD test. The hydrogen evolution rate of CT-WE43 is ~ 0.6 $ml/cm^2 \cdot hr$, comparable to those reported for the same alloy elsewhere [54], and those of AD-WE43 sample is ~ 0.02 $ml/cm^2 \cdot hr$, comparable to the values reported for magnetron sputtered Mg-Y alloys immersed in 3.5% NaCl solution at 25 ^oC [38].

3.5. Nature of the surface layer

Figure 8 shows the surface morphologies and EDS analysis of both alloys after immersion in BBBS for 4 hours. This relative short duration of immersion was chosen to

ensure AD-WE43 was not completely dissolved due its limited thickness and high corrosion rate. The surface morphology of CT-WE43 showed a thick corrosion product film with extensive cracks, similar to that reported for the same alloy in Ringer's solution, cell culture and simulated body fluid [44, 47]. EDS maps in Figure 8 (a) shows that the corrosion film on CT-WE43 were enriched in Zr and Y. In contrast, the surface of AD-WE43 was still smooth without noticeable corrosion product formation (Figure 8(b)). The corresponding EDS maps indicated that all the alloying elements remained in solution after 4 hours exposure. Figure 9 shows the cross-sections of corroded samples. While the CT-WE43 shows cracks of ~ 1.65 μm deep, the AD-WE43 exhibited a uniform thickness (with reduced overall thickness) after 4 hrs immersion test.

To characterize this surface layer, surface XPS analysis of both samples, before and after corrosion tests was performed, as shown in Figure 10. It can be seen that after corrosion, Mg and Y peaks shifted towards higher binding energy values for both samples, indicating that Mg and Y were oxidized to become MgO, and Y_2O_3, respectively. In addition, a high P content was observed in the corroded AD-WE43, but not in CT-WE43. The observed shift in binding energy is an indicative of the formation of MgO layer on both alloys after exposure to BBBS, similar to that encountered in WE43 Mg alloys exposed to acellular SBF, cell culture medium, and Ringer's solutions with pH range of (7.2 – 7.8) [8, 44, 47, 55]. The presence of Y in the outermost layer of the AD-WE43 before and after exposure in its metallic and oxide states, respectively, indicated that alloys produced by magnetron sputtering in this work has the advantages of not altering the global composition of WE43 Mg alloys, similar to that observed in Ti ion implanted WE43 alloys [8].

To further evaluate the structure and thickness of the corrosion layer, cross-sectional TEM analysis were carried out for both alloys after immersion in BBBS for 90 min. The cross-sectional TEM sample of the corroded cast alloy was prepared by the standard FIB lift-out method. The lift-out location was selected from a representative region showing clear evidence of corrosion product formation, yet away from the cracks (Figure 11.a). To protect the surface layers from Ga ion beam damage during milling, a ~ 50 nm carbon film was first deposited by e-beam evaporation followed by ion beam deposition of a Pt layer of 1-3 μm. Figure 11(b-d) shows that ~ 33.6 ± 15.8 nm thick

surface oxidation layer was formed on the corroded CT-WE43. To reveal the crystal nature of this layer, SAD was performed at three locations: the top (right below the surface), middle (~ 10 nm below the surface), and bottom (~ 15 nm below the surface), as shown in Figure 12. The analysis of SAD patterns resulted in lattice constant (d_{111} = 2.431 Å) that is indicative of the formation of MgO and the absence of $Mg(OH)_2$ in all three locations, consistent with the prior XPS results.

Cross-sectional TEM samples of the corroded AD-WE43 were prepared from an arbitrary location on the surface as no apparent corrosion product was detected on the whole surface, as indicated in Figure 13(a). The inset in Figure 13(a) shows that extensive grooves were formed on the surface, with average spacing of 84 ± 15 nm, similar to the size of the surface nodules (~ 91 ± 20 nm) in Figure 1(b). Fig. 13(b) shows that these groves, ~ 200-300 nm deep and 252 ± 86 nm wide, formed preferentially along the colony boundaries. In deposited nanocrystalline metallic thin films, the presence of surface nodules have been widely reported, where the characteristic width of the surface nodule, w_c, is often orders of magnitude higher than the grain size d [56]. These colonies, which are often composed of crystallographically related grains, grow competitively during thin film growth. For example, Ruan and Schuh [56] showed that the intercolony boundaries of electrodeposited Ni-W are chemically and structurally different from the colony interior due to preferred segregation of W at the boundaries, resulting in their highly susceptibility to etching and cracking. In our study, a similar mechanism might also be present that result in preferred corrosion of the intercolony boundaries. In contrast to the cast alloy, the HRTEM image of the AD-WE43 (Figure 13(c)) did not reveal the formation of a well-defined oxidation layer of corrosion products. Instead continuous atomic planes were clearly observed from the outermost surface to the sample interior. The absence of a well-defined corrosion product layer was also revealed by the electron diffraction analysis (Figure 13(d)), where the diffraction pattern of the outermost surface layer is formed from a crystalline Mg phase only.

The composition of the corroded surfaces of both samples was further studied by STEM-EDS analysis. Representative results are shown in Figure 14. The corrosion product of the CT-WE43 was found to have darker contrast compared to both the underneath alloy and protective layers, while the AD-WE43 showed homogeneous metal

layer adjacent to the protective layer. In the corrosion product layer (~ 40 nm) of the corroded CT-WE43 (Figure 14(b)), a higher O, Zr and Y content were detected, as compared to the interior. On the other hand, a well-defined oxide layer was not detected in AD-WE43 after corrosion, despite a slight increase of O content ~ 20 nm below the surface.

The composition, structure, and thickness of the corrosion product have profound effect on the corrosion behavior of Mg. Yet the nature of the corrosion product formed on Mg alloys was often found to be complex and highly sensitive to pH and corrosion conditions. Typically, MgO and $Mg(OH)_2$ are observed in the surface films of corroded Mg alloys. For example, Taheri et. al [57] found that the corrosion product of commercially pure Mg exposed to water is composed of a bi-layer structure. Other studies showed that the inner layer is rich in MgO, while the outer layer is rich in $Mg(OH)_2$. XPS and ToF SIMS analysis of mechanically polished Mg alloys aged in water showed that the inner layer was formed due to the reaction with oxygen gas, while the outer layer was formed due to the hydration of MgO [58-60]. On the other hand, Unocic et al. [61] found that pure Mg samples exposed to DI water for 4 hours did not show the formation of $Mg(OH)_2$ layer, this layer appeared after 24 hours of exposure. In the current study, due to the limited sample thickness of the as-deposited alloy, immersion tests were terminated after 4 hrs, which could explain the absence of $Mg(OH)_2$ on the outermost surface of both alloys.

In terms of the MgO layer formation on the surface, contradictory results have been reported. For example, Nordlien et al. [62] found that an inner, dense, and amorphous MgO layer was formed naturally on a fresh Mg surface exposed to humid air and water, whereas Taheri et. al [57] reported the formation of porous and nano-crystalline MgO inner layer. Our study indicated the formation of nanocrystalline MgO layer on the cast alloy, which is likely a result of the oxidation of Mg following the sequence; oxygen chemisorption, random assembly into islands and subsequent lateral growth, oxide formation, and finally thickening [63]. Chu and Marquis [51] found that for a commercial WE43 Mg alloy exposed to 3.5 wt% NaCl solution at pH ~ 10, a bi-layered corrosion product formed consisting of a porous of $Mg(OH)_2$ outer layer and compact crystalline MgO inner layer. While prior studies offer some knowledge of surface film formation in coarse grained WE43 Mg alloy, to the best of our knowledge, that of nanocrystalline

WE43 alloy is not yet reported. The TEM and XPS study presented in this work, coupled with disturbed E_{OC} measurements, indicate that a delicate, easily disrupted and self-repairing surface oxide layer is present on the as-deposited nanocrystalline alloy, which dramatically slows down the anodic reaction kinetics of Mg. The presence of this MgO surface layer was revealed by XPS and STEM-EDS line scans, although its thickness is too small to be directly measured by cross-sectional TEM analysis. The formation of this quasi-stable protective surface layer is believed to be related to the nanocrystalline nature of the thin film. Nanocrystallization has often been found to be associated with enhanced corrosion resistance in steel, Ni-based alloys [64], and Mg alloys [65]. The small grain sizes promote uniform element distribution of alloying elements, which facilitates rapid formation of compact oxide layer, promote the diffusion of passive elements in the surface layer, and reduces the adsorption of Cl^- on the surface [64, 66]. For example, deposited nanocrystalline Mg-Ti, Mg-Cu-Y, Mg-Ni-Nd exhibit a distinct passive region when anodically polarized in dilute chloride solution at pH of ~ 10-12 [65, 67]. On the other hand, the preferred corrosion of the colony boundaries of the thin film sample suggested that the dominating corrosion mechanism is the micro-galvanic coupling between the colony boundaries (anode) and interior (cathode), likely resulting from their chemical and structural differences. Indeed, even in a non-equilibrium process such as PVD, there is still a thermodynamic driving force for the non-soluble alloying elements to segregate at grain/colony boundaries. For example, Griguceviciene et al. [68] reported the transition from a solid solution to dual phase in PVD deposited Mg-Al-Zr when Zr concentration was increased to ~ 50 at. %. More detailed characterization of the chemical composition of the colony boundary can be performed using atom probe tomography, which is left for future work. Finally, Figure 15 summarizes the corrosion mechanism of the cast and as-deposited WE43 alloy studied here. In the phase separated cast alloy, micro-galvanic coupling between the α-Mg and (Zr,Y)-rich precipitates dominate the corrosion process; a discontinuous corrosion product layer forms on the surface with a high MgO content. In the chemically homogenous as-deposited alloy, and due to the elimination of precipitates, the dominating corrosion mechanism seemed to be the micro-galvanic coupling between the colony boundaries and interior; the surface oxide layer is thin and delicate, but self-repairing upon local disruption.

4. Summary and conclusions

This study showed that proper microstructure modification including minimizing precipitation and formation of a chemically homogeneous supersaturated solid solution with an average grain size of ~ 46 nm led to a reduction of corrosion rate of WE43 alloy by more than one order of magnitude compared to the conventionally cast alloy. It is believed that minimizing precipitates led to significantly reduced cathode size hence, slowed down the cathodic reaction kinetics, while the formation of a somewhat protective surface layer on the as-deposited alloy slowed down the anodic reaction kinetics. Post-corrosion surface characterizations of the cast alloy revealed that corrosion products were primarily formed above areas enriched in Zr and Y elements and exhibited a network of dehydration cracks, through which the corrosive media could penetrate towards the interior of the sample. In contrast, the as-deposited alloy managed to maintain the chemical homogeneity of the pre-corrosion condition. Corrosion was found to proceed in a more uniform fashion in the as-deposited sample due to the formation of protective surface layer. Finally, it is understood that while physical vapor deposition is a convenient non-equilibrium processing technique to tailor alloy microstructure, it is however a surface technique and in its laboratory form not suitable for producing millimeter sized bulk samples. Nevertheless the understanding generated will provide critical design guidance for microstructure optimization in bulk samples produced by other scalable non-equilibrium techniques such as semi-solid casting, rapid solidification, cold spray, electrodeposition, powder metallurgy, etc. Such scale-up experiments and industrial development are left for future research.

5. Acknowledgements

This research was financially supported by ConMed Corporation and the National Science Foundation under Grant DMR-1856196. The authors thankfully acknowledge the discussion of results with Kimmo Lähteenkorva and Christopher Stahle from ConMed Corporation and Dr. Alberto A. Sagüés from University of South Florida. H.M acknowledges the assistance of Nicholas G. Rudawski from the University of Florida for XPS analysis. The sample preparation and most materials characterization were

performed at the Nano Research and Educational Center (NREC) at the University of South Florida. XPS analysis was performed at the University of Florida.

References

[1] R. Waksman, R. Pakala, P.K. Kuchulakanti, R. Baffour, D. Hellinga, R. Seabron, F.O. Tio, E. Wittchow, S. Hartwig, C. Harder, R. Rohde, B. Heublein, A. Andreae, K.H. Waldmann, A. Haverich, Safety and efficacy of bioabsorbable magnesium alloy stents in porcine coronary arteries, Catheterization and Cardiovascular Interventions 68(4) (2006) 607-617.
[2] B. Heublein, R. Rohde, V. Kaese, M. Niemeyer, W. Hartung, A. Haverich, Biocorrosion of magnesium alloys: a new principle in cardiovascular implant technology?, Heart 89(6) (2003) 651-656.
[3] W. Jin, G. Wu, H. Feng, W. Wang, X. Zhang, P.K. Chu, Improvement of corrosion resistance and biocompatibility of rare-earth WE43 magnesium alloy by neodymium self-ion implantation, Corrosion Science 94 (2015) 142-155.
[4] F. Witte, J. Fischer, J. Nellesen, H.-A. Crostack, V. Kaese, A. Pisch, F. Beckmann, H. Windhagen, In vitro and in vivo corrosion measurements of magnesium alloys, Biomaterials 27(7) (2006) 1013-1018.
[5] C. Castellani, R.A. Lindtner, P. Hausbrandt, E. Tschegg, S.E. Stanzl-Tschegg, G. Zanoni, S. Beck, A.-M. Weinberg, Bone–implant interface strength and osseointegration: Biodegradable magnesium alloy versus standard titanium control, Acta Biomaterialia 7(1) (2011) 432-440.
[6] A. Weiler, R.F.G. Hoffmann, A.C. Stähelin, H.-J. Helling, N.P. Südkamp, Biodegradable Implants in Sports Medicine: The Biological Base, Arthroscopy: The Journal of Arthroscopic & Related Surgery 16(3) (2000) 305-321.
[7] M.P. Staiger, A.M. Pietak, J. Huadmai, G. Dias, Magnesium and its alloys as orthopedic biomaterials: A review, Biomaterials 27(9) (2006) 1728-1734.
[8] Y. Zhao, G. Wu, Q. Lu, J. Wu, R. Xu, K.W.K. Yeung, P.K. Chu, Improved surface corrosion resistance of WE43 magnesium alloy by dual titanium and oxygen ion implantation, Thin Solid Films 529 (2013) 407-411.
[9] W. Jin, G. Wu, P. Li, P.K. Chu, Improved corrosion resistance of Mg-Y-RE alloy coated with niobium nitride, Thin Solid Films 572 (2014) 85-90.
[10] N. Liu, J. Wang, L. Wang, Y. Wu, L. Wang, Electrochemical corrosion behavior of Mg–5Al–0.4Mn–xNd in NaCl solution, Corrosion Science 51(6) (2009) 1328-1333.
[11] Y. Zhao, M.I. Jamesh, W.K. Li, G. Wu, C. Wang, Y. Zheng, K.W.K. Yeung, P.K. Chu, Enhanced antimicrobial properties, cytocompatibility, and corrosion resistance of plasma-modified biodegradable magnesium alloys, Acta Biomaterialia 10(1) (2014) 544-556.
[12] F. Feyerabend, J. Fischer, J. Holtz, F. Witte, R. Willumeit, H. Drücker, C. Vogt, N. Hort, Evaluation of short-term effects of rare earth and other elements used in magnesium alloys on primary cells and cell lines, Acta Biomaterialia 6(5) (2010) 1834-1842.
[13] G. Song, Control of biodegradation of biocompatable magnesium alloys, Corrosion Science 49(4) (2007) 1696-1701.
[14] Y. Xin, T. Hu, P.K. Chu, In vitro studies of biomedical magnesium alloys in a simulated physiological environment: A review, Acta Biomaterialia 7(4) (2011) 1452-1459.
[15] A. Atrens, M. Liu, N.I. Zainal Abidin, Corrosion mechanism applicable to biodegradable magnesium implants, Materials Science and Engineering B: Solid-State Materials for Advanced Technology 176(20) (2011) 1609-1636.
[16] N.T. Kirkland, G. Williams, N. Birbilis, Observations of the galvanostatic dissolution of pure magnesium, Corrosion Science 65 (2012) 5-9.

[17] F. Witte, V. Kaese, H. Haferkamp, E. Switzer, A. Meyer-Lindenberg, C.J. Wirth, H. Windhagen, In vivo corrosion of four magnesium alloys and the associated bone response, Biomaterials 26(17) (2005) 3557-3563.
[18] G.S. Frankel, A. Samaniego, N. Birbilis, Evolution of hydrogen at dissolving magnesium surfaces, Corrosion Science 70 (2013) 104-111.
[19] S. Thomas, N.V. Medhekar, G.S. Frankel, N. Birbilis, Corrosion mechanism and hydrogen evolution on Mg, Current Opinion in Solid State and Materials Science 19(2) (2015) 85-94.
[20] K. Gusieva, C. Davies, J. Scully, N. Birbilis, Corrosion of magnesium alloys: the role of alloying, International Materials Reviews 60(3) (2015) 169-194.
[21] Y. Ding, C. Wen, P. Hodgson, Y. Li, Effects of alloying elements on the corrosion behavior and biocompatibility of biodegradable magnesium alloys: a review, Journal of materials chemistry B 2(14) (2014) 1912-1933.
[22] L.L. Rokhlin, Magnesium alloys containing rare earth metals: structure and properties, Crc Press2003.
[23] J.M. Seitz, R. Eifler, J. Stahl, M. Kietzmann, F.W. Bach, Characterization of MgNd2 alloy for potential applications in bioresorbable implantable devices, Acta Biomaterialia 8(10) (2012) 3852-3864.
[24] Q. Wang, W. Jin, G. Wu, Y. Zhao, X. Jin, X. Hu, J. Zhou, G. Tang, P.K. Chu, Rare-earth-incorporated polymeric vector for enhanced gene delivery, Biomaterials 35(1) (2014) 479-488.
[25] T. Zhang, G. Meng, Y. Shao, Z. Cui, F. Wang, Corrosion of hot extrusion AZ91 magnesium alloy. Part II: Effect of rare earth element neodymium (Nd) on the corrosion behavior of extruded alloy, Corrosion Science 53(9) (2011) 2934-2942.
[26] T. Takenaka, T. Ono, Y. Narazaki, Y. Naka, M. Kawakami, Improvement of corrosion resistance of magnesium metal by rare earth elements, Electrochimica Acta 53(1) (2007) 117-121.
[27] R. Arrabal, E. Matykina, A. Pardo, M.C. Merino, K. Paucar, M. Mohedano, P. Casajús, Corrosion behaviour of AZ91D and AM50 magnesium alloys with Nd and Gd additions in humid environments, Corrosion Science 55 (2012) 351-362.
[28] F. Witte, N. Hort, C. Vogt, S. Cohen, K.U. Kainer, R. Willumeit, F. Feyerabend, Degradable biomaterials based on magnesium corrosion, Current Opinion in Solid State and Materials Science 12(5–6) (2008) 63-72.
[29] J. Zhang, J. Wang, X. Qiu, D. Zhang, Z. Tian, X. Niu, D. Tang, J. Meng, Effect of Nd on the microstructure, mechanical properties and corrosion behavior of die-cast Mg–4Al-based alloy, Journal of Alloys and Compounds 464(1–2) (2008) 556-564.
[30] G.L. Song, A. Atrens, Corrosion mechanisms of magnesium alloys, Adv Eng Mater 1(1) (1999) 11-33.
[31] Y.W. Song, D.Y. Shan, E.H. Han, Pitting corrosion of a Rare Earth Mg alloy GW93, J Mater Sci Technol 33(9) (2017) 954-960.
[32] X.B. Zhang, G.Y. Yuan, L. Mao, J.L. Niu, W.J. Ding, Biocorrosion properties of as-extruded Mg-Nd-Zn-Zr alloy compared with commercial AZ31 and WE43 alloys, Mater Lett 66(1) (2012) 209-211.
[33] J. Trinidad, G. Arruebarrena, I. Marco, I. Hurtado, E.S. de Argandona, Effectivity of fluoride treatment on hydrogen and corrosion product generation in temporal implants for different magnesium alloys, P I Mech Eng H 227(12) (2013) 1301-1311.
[34] H.S. Jiang, M.Y. Zheng, X.G. Qiao, K. Wu, Q.Y. Peng, S.H. Yang, Y.H. Yuan, J.H. Luo, Microstructure and mechanical properties of WE43 magnesium alloy fabricated by direct-chill casting, Materials Science and Engineering: A 684 (2017) 158-164.
[35] C. Liu, Q. Li, J. Liang, J. Zhou, L. Wang, Microstructure and corrosion behaviour of laser surface melting treated WE43 magnesium alloy, RSC Advances 6(36) (2016) 30642-30651.
[36] A. Mazor, D.J. Srolovitz, P.S. Hagan, Bukiet, G. B, Columnar growth in thin films, Physical Review Letters 60(5) (1988) 424-427.
[37] T. Rzychoń, A. Kiełbus, Microstructure of WE43 casting magnesium alloys, Journal of Achievements in Materials and Manufacturing Engineering 21(1) (2007) 31-34.

[38] K. Schlüter, Z. Shi, C. Zamponi, F. Cao, E. Quandt, A. Atrens, Corrosion performance and mechanical properties of sputter-deposited MgY and MgGd alloys, Corrosion Science 78 (2014) 43-54.
[39] C. Blawert, V. Heitmann, W. Dietzel, M. Störmer, Y. Bohne, S. Mändl, B. Rauschenbach, Corrosion properties of supersaturated magnesium alloy systems, Materials Science Forum, 2007, pp. 1679-1684.
[40] G. Garces, M.C. Cristina, M. Torralba, P. Adeva, Texture of magnesium alloy films growth by physical vapour deposition (PVD), Journal of Alloys and Compounds 309(1-2) (2000) 229-238.
[41] L.G. Bland, A.D. King, N. Birbilis, J.R. Scully, Assessing the Corrosion of Commercially Pure Magnesium and Commercial AZ31B by Electrochemical Impedance, Mass-Loss, Hydrogen Collection, and Inductively Coupled Plasma Optical Emission Spectrometry Solution Analysis, Corrosion 71(2) (2015) 128-145.
[42] A.D. Sudholz, K. Gusieva, X.B. Chen, B.C. Muddle, M.A. Gibson, N. Birbilis, Electrochemical behaviour and corrosion of Mg–Y alloys, Corrosion Science 53(6) (2011) 2277-2282.
[43] N. Birbilis, G. Williams, K. Gusieva, A. Samaniego, M.A. Gibson, H.N. McMurray, Poisoning the corrosion of magnesium, Electrochemistry Communications 34 (2013) 295-298.
[44] M. Jamesh, G. Wu, Y. Zhao, P.K. Chu, Effects of silicon plasma ion implantation on electrochemical corrosion behavior of biodegradable Mg–Y–RE Alloy, Corrosion Science 69 (2013) 158-163.
[45] T. Cain, L. Bland, N. Birbilis, J. Scully, A compilation of corrosion potentials for magnesium alloys, Corrosion 70(10) (2014) 1043-1051.
[46] E. McCafferty, Validation of corrosion rates measured by the Tafel extrapolation method, Corrosion Science 47(12) (2005) 3202-3215.
[47] M.I. Jamesh, G. Wu, Y. Zhao, W. Jin, D.R. McKenzie, M.M.M. Bilek, P.K. Chu, Effects of zirconium and nitrogen plasma immersion ion implantation on the electrochemical corrosion behavior of Mg–Y–RE alloy in simulated body fluid and cell culture medium, Corrosion Science 86 (2014) 239-251.
[48] A.D. King, N. Birbilis, J.R. Scully, Accurate Electrochemical Measurement of Magnesium Corrosion Rates; a Combined Impedance, Mass-Loss and Hydrogen Collection Study, Electrochimica Acta 121 (2014) 394-406.
[49] A. Pardo, S. Feliu, M.C. Merino, R. Arrabal, E. Matykina, Electrochemical Estimation of the Corrosion Rate of Magnesium/Aluminium Alloys, International Journal of Corrosion 2010 (2010).
[50] R.L. Petty, A.W. Davidson, J. Kleinberg, The Anodic Oxidation of Magnesium Metal: Evidence for the Existence of Unipositive Magnesium1,2, Journal of the American Chemical Society 76(2) (1954) 363-366.
[51] P.W. Chu, E.A. Marquis, Linking the microstructure of a heat-treated WE43 Mg alloy with its corrosion behavior, Corros Sci 101 (2015) 94-104.
[52] A.C. Vieira, L.A. Rocha, N. Papageorgiou, S. Mischler, Mechanical and electrochemical deterioration mechanisms in the tribocorrosion of Al alloys in NaCl and in NaNO3 solutions, Corros Sci 54 (2012) 26-35.
[53] R. Harrison, D. Maradze, S. Lyons, Y.F. Zheng, Y. Liu, Corrosion of magnesium and magnesium-calcium alloy in biologically-simulated environment, Prog Nat Sci-Mater 24(5) (2014) 539-546.
[54] N. Li, Y. Zheng, Novel Magnesium Alloys Developed for Biomedical Application: A Review, J Mater Sci Technol 29(6) (2013) 489-502.
[55] M.I. Jamesh, G. Wu, Y. Zhao, D.R. McKenzie, M.M.M. Bilek, P.K. Chu, Electrochemical corrosion behavior of biodegradable Mg–Y–RE and Mg–Zn–Zr alloys in Ringer's solution and simulated body fluid, Corrosion Science 91 (2015) 160-184.
[56] S. Ruan, C.A. Schuh, Mesoscale structure and segregation in electrodeposited nanocrystalline alloys, Scripta Mater 59(11) (2008) 1218-1221.
[57] M. Taheri, R. Phillips, J. Kish, G. Botton, Analysis of the surface film formed on Mg by exposure to water using a FIB cross-section and STEM–EDS, Corrosion Science 59 (2012) 222-228.
[58] H.B. Yao, Y. Li, A.T.S. Wee, An XPS investigation of the oxidation/corrosion of melt-spun Mg, Appl Surf Sci 158(1) (2000) 112-119.
[59] V. Fournier, P. Marcus, I. Olefjord, Oxidation of magnesium, Surface and Interface Analysis 34(1) (2002) 494-497.

[60] A. Seyeux, M. Liu, P. Schmutz, G. Song, A. Atrens, P. Marcus, ToF-SIMS depth profile of the surface film on pure magnesium formed by immersion in pure water and the identification of magnesium hydride, Corrosion Science 51(9) (2009) 1883-1886.
[61] K.A. Unocic, H.H. Elsentriecy, M.P. Brady, H. Meyer, G. Song, M. Fayek, R.A. Meisner, B. Davis, Transmission electron microscopy study of aqueous film formation and evolution on magnesium alloys, Journal of The Electrochemical Society 161(6) (2014) C302-C311.
[62] J.H. Nordlien, S. Ono, N. Masuko, K. Nisancioglu, A TEM investigation of naturally formed oxide films on pure magnesium, Corrosion Science 39(8) (1997) 1397-1414.
[63] H. Namba, J. Darville, J.M. Gilles, A model for the oxidation of Mg(0001) based upon LEED, AES, ELS and work function measurements, Surface Science 108(3) (1981) 446-482.
[64] L. Liu, Y. Li, F.H. Wang, Electrochemical Corrosion Behavior of Nanocrystalline Materials-a Review, J Mater Sci Technol 26(1) (2010) 1-14.
[65] F.Y. Cao, G.L. Song, A. Atrens, Corrosion and passivation of magnesium alloys, Corros Sci 111 (2016) 835-845.
[66] S. Gollapudi, Grain size distribution effects on the corrosion behaviour of materials, Corrosion Science 62 (2012) 90-94.
[67] G.L. Song, K.A. Unocic, M. Harry, E. Cakmak, M.P. Brady, P.E. Gannon, P. Himmer, Q. Andrews, The corrosion and passivity of sputtered Mg-Ti alloys, Corros Sci 104 (2016) 36-46.
[68] A. Grigucevicience, K. Leinartas, R. Juskenas, E. Juzeliunas, Structure and initial corrosion resistance of sputter deposited nanocrystalline Mg-Al-Zr alloys, Mat Sci Eng a-Struct 394(1-2) (2005) 411-416.

Tables and Figures

Table 1. Summary of the global and precipitate compositions of cast and as-sputtered Mg-WE43, measured by EDS analysis on polished sample surfaces. All values are reported as average (range).

	Mg (wt.%)	Y (wt.%)	Nd (wt.%)	Zr (wt.%)
Cast WE43 (global)	93.1 (0.6)	3.6 (0.9)	2.4 (0.4)	0.6 (0.4)
Longitudinal/Spherical phase	82.4 (8.1)	6.6 (6.78)	7.2 (5.1)	3.9 (1.5)
Cuboidal phase	69.1 (12.4)	9.2 (3.8)	3.5 (3.8)	18.1 (7.7)
As-deposited WE43 (global)	93.1 (0.9)	4.7 (0.5)	1.8 (0.3)	0.5 (0.2)

Table 2. Electrochemical parameters obtained from PD and EIS tests of cast and as-deposited WE43 alloy. All values are reported as average (range).

Samples	E_{oc} (mV vs. Ag/AgCl)	βc (mV/decade)	Nominal i_{corr} (μA/cm²) measured from PD tests	Nominal i_{corr} (μA/cm²) measured from EIS tests
Cast	-1510 (50)	250 (20)	100 (20)	110 (15)
As-deposited	-1520 (50)	350 (50)	12 (2)	7 (1.5)

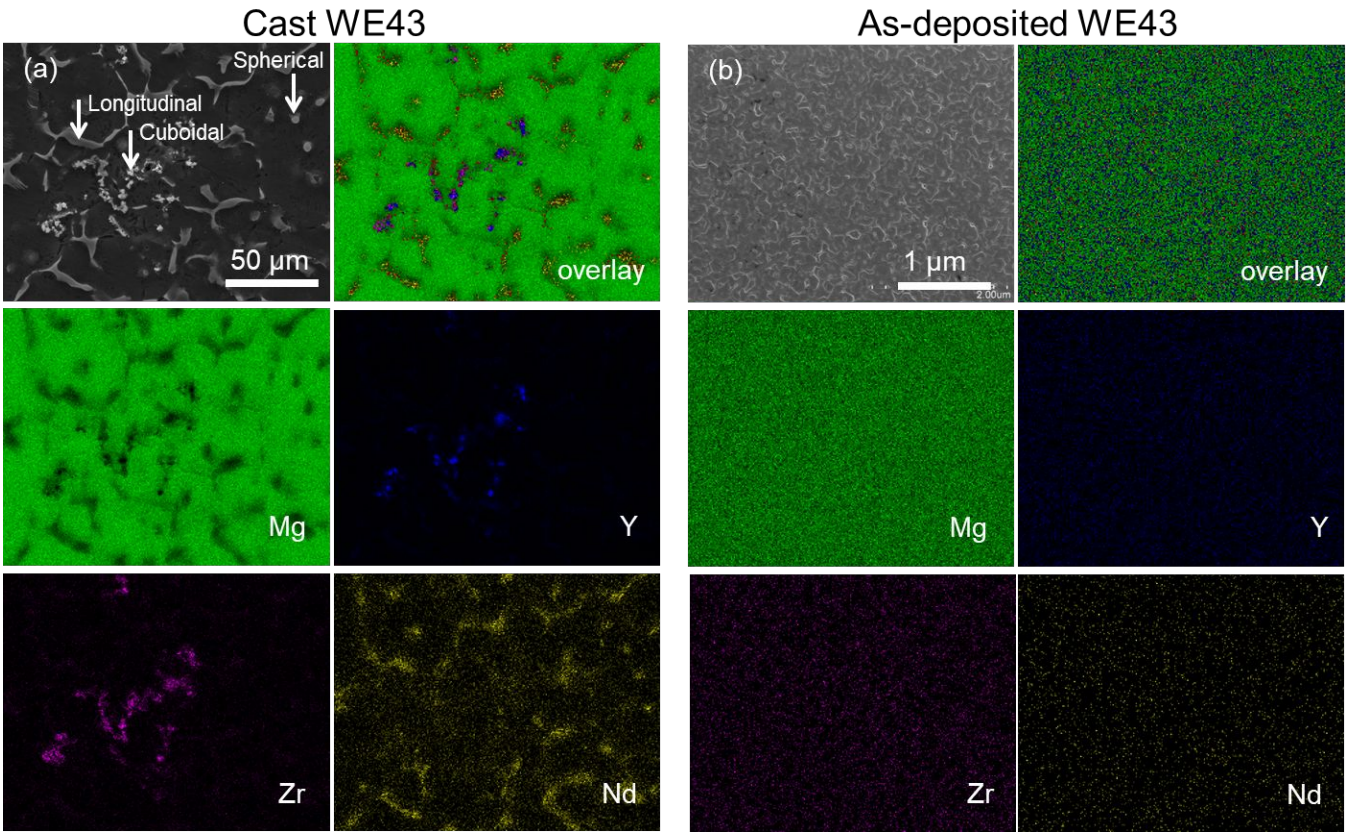

Figure 1. Surface SEM image and the corresponding EDS element maps of (a) cast and (b) as-deposited WE43 Mg alloy.

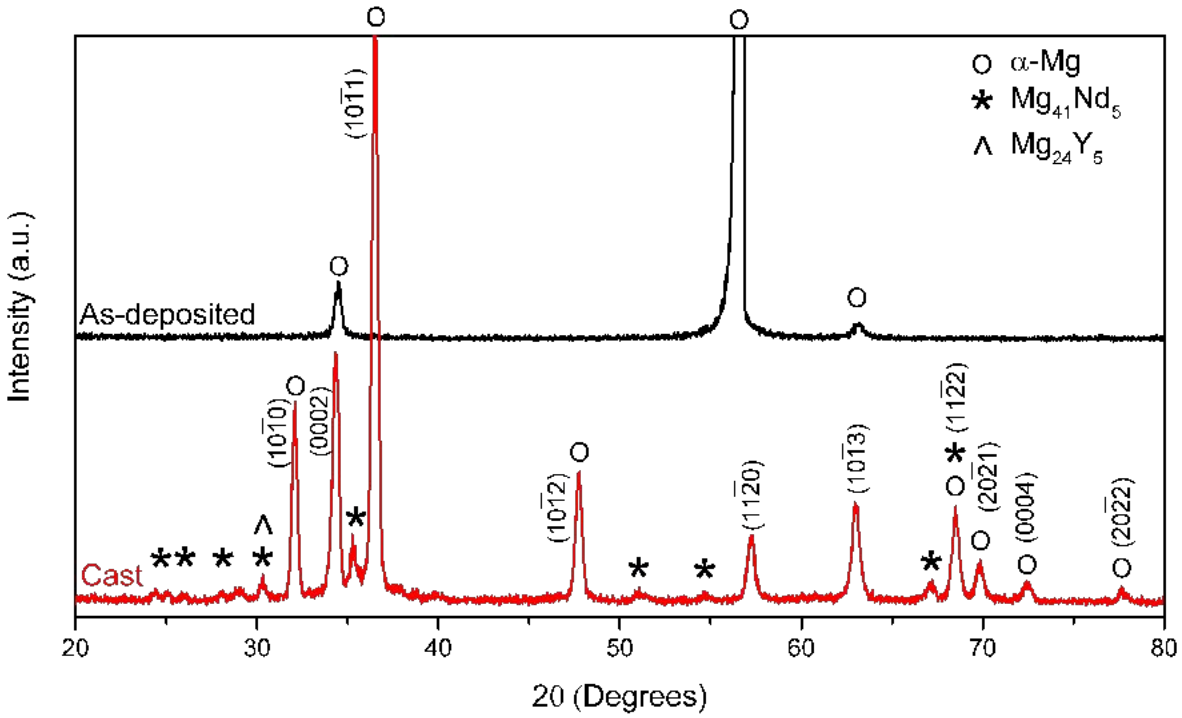

Figure 2. GIXRD of cast (red) and as-deposited (black) WE43 Mg alloy.

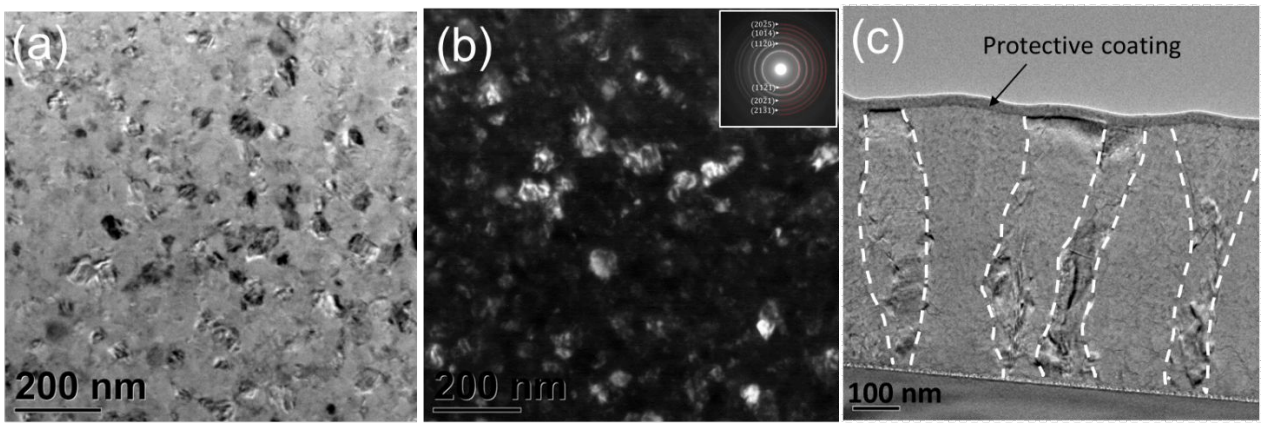

Figure 3. (a) Bright field (BF), (b) dark field (DF) TEM images of plane-view samples, and (c) BF TEM image of cross-sectional sample of as-deposited WE43 Mg alloy. The inset in (b) shows the corresponding SAD pattern of image (b). Dashed lines in (c) indicate grain boundaries.

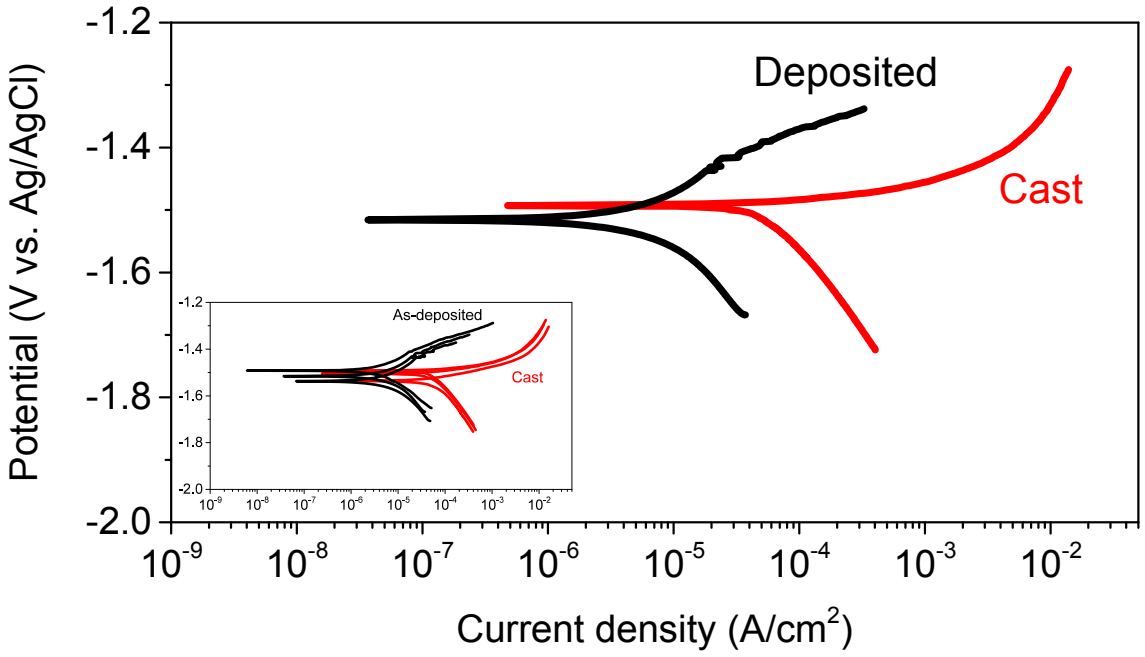

Figure 4. Representative Tafel plots of cast (red) and as-deposited (black) WE43 Mg alloy from PD tests after immersion in BBBS for 20 min. Inset show PD results from three separate tests for each sample sets.

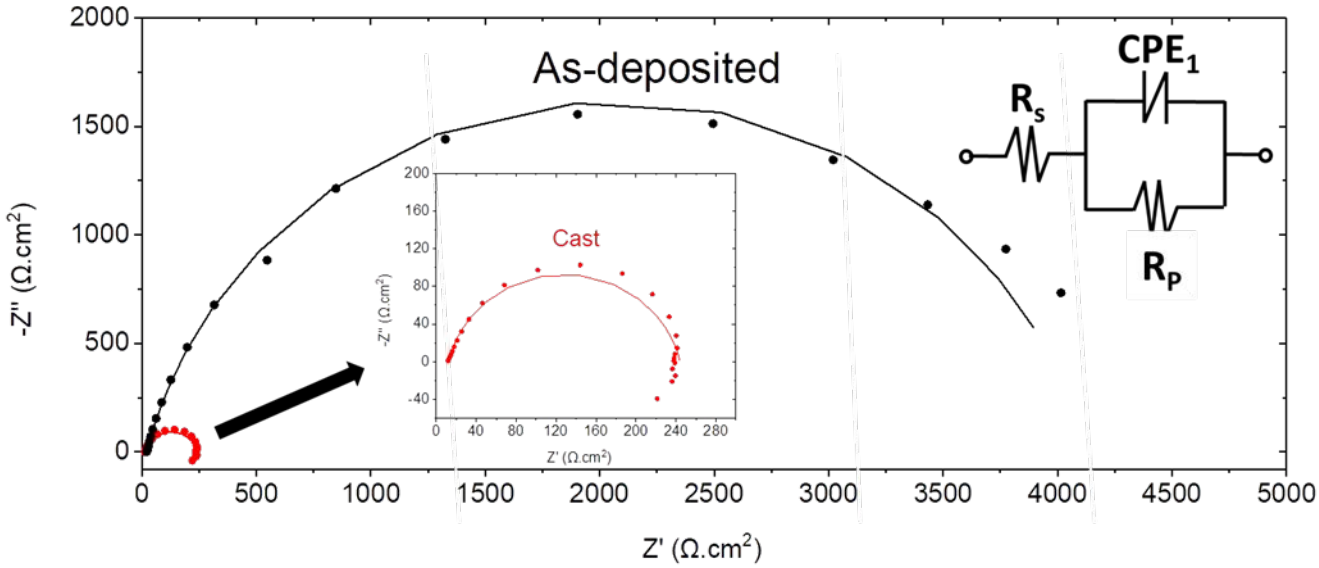

Figure 5. Representative Nyquist plots (scattered data) of cast and as-deposited WE43 Mg alloy conducted after E_{OC} stabilization for 15 min in BBBS. The top right inset shows the equivalent circuit model used to fit the experimental data, as represented by the solid lines in the Nyquist plots.

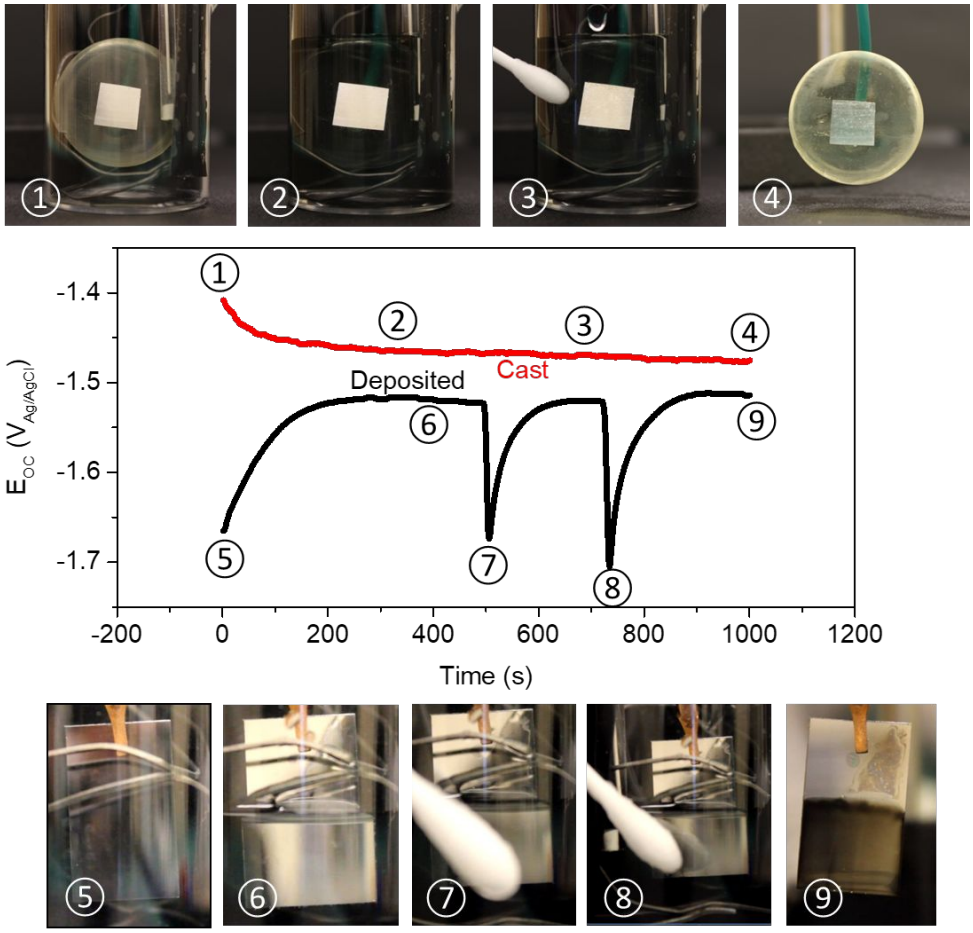

Figure 6. Evolution of E_{OC} during immersion test in blood bank buffered saline. A Q-tip was used to gently scrub the surface at time 2 and 3 for the cast sample, and at time 7 and 8 for the deposited sample, as labeled in the figure.

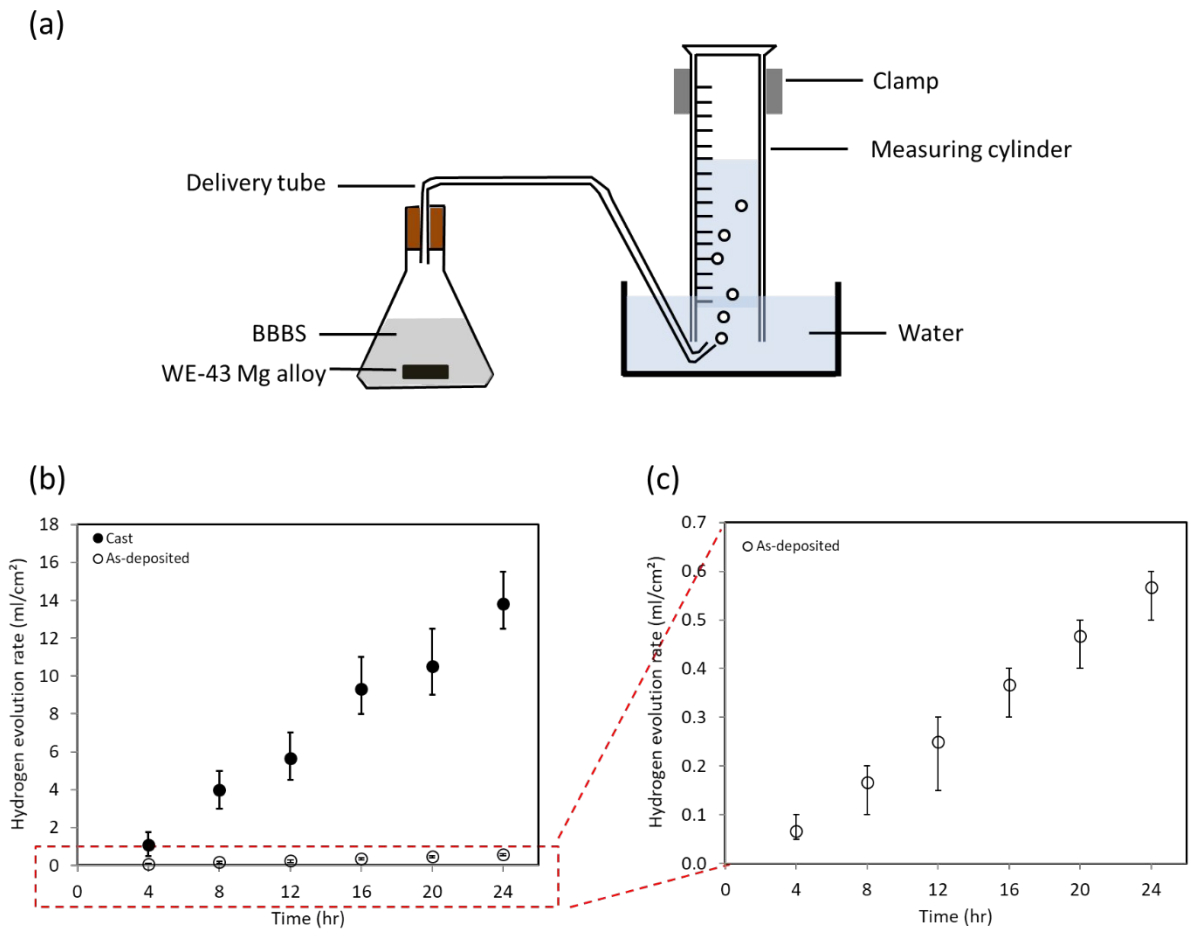

Figure 7. (a) Schematic illustration of hydrogen measurement setup during immersion test. Hydrogen evolution rate of (b) both and (c) as-deposited WE43 taken during immersion tests of 24 hrs in BBBS.

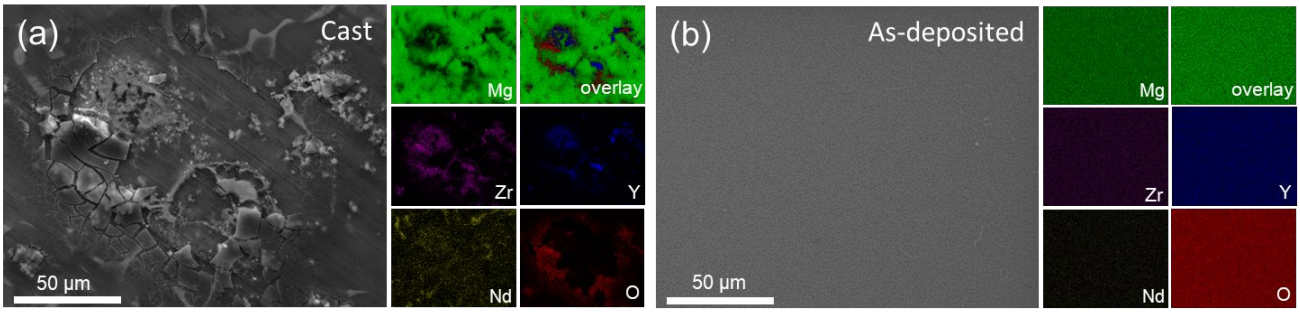

Figure 8. Surface SEM image and the corresponding element maps of (a) cast and (b) as-deposited WE43 Mg alloy after immersion test for 4 hours.

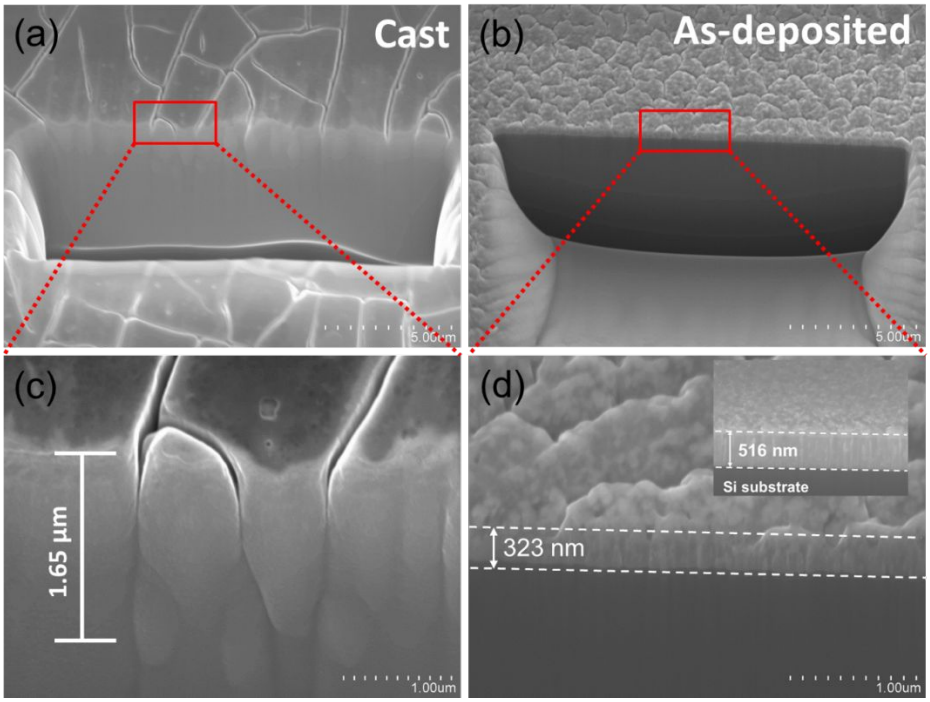

Figure 9. Cross-sectional SEM images of (a and c) cast, and (b and d) as-deposited WE43 Mg alloy after immersion test for 4 hours. Images (c) and (d) are enlarged from the box area in (a) and (b) respectively. In image (d), the bottom dark area corresponds to a Si substrate.

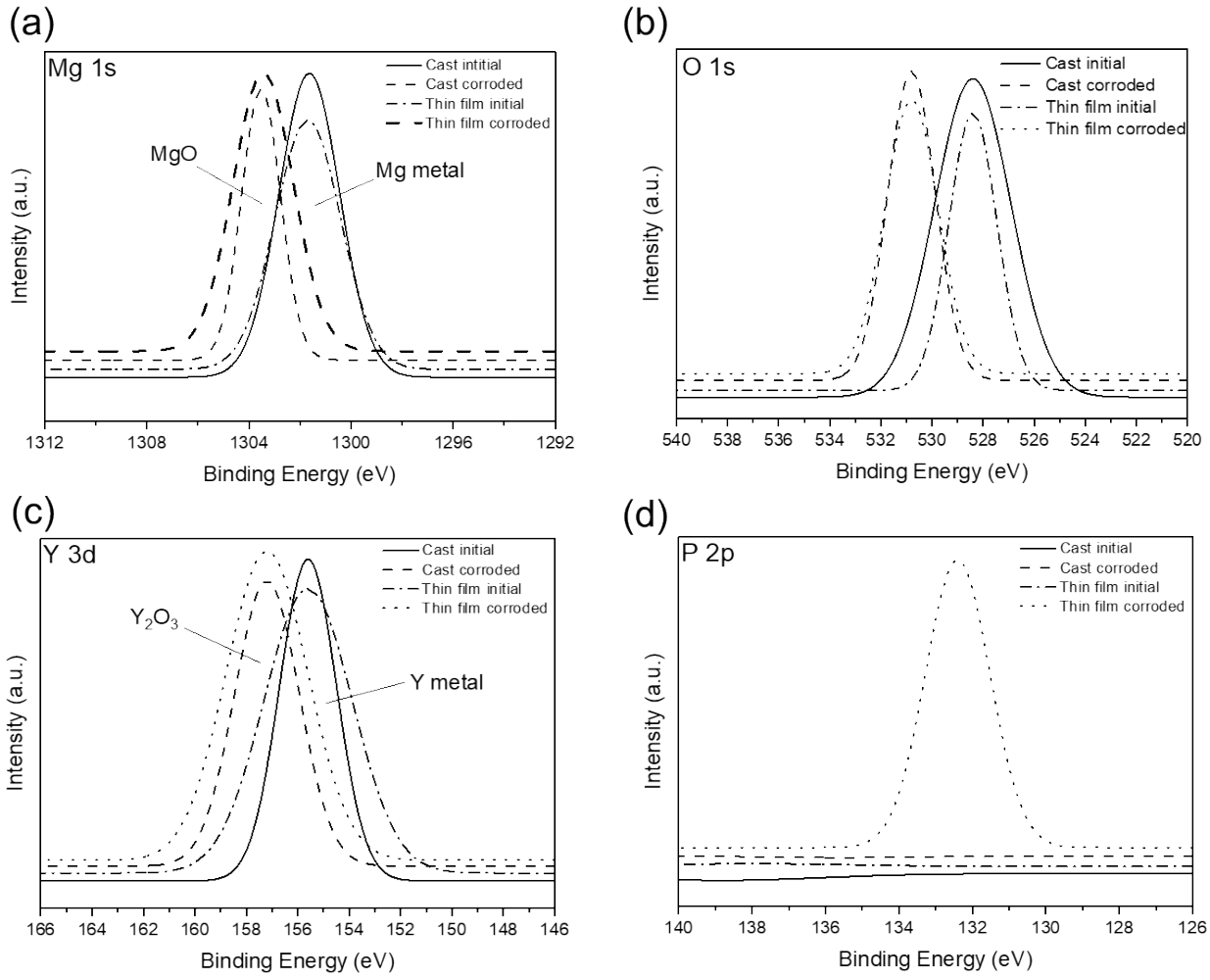

Figure 10. XPS spectra of (a) Mg, (b) O 1s, (c) Y 3d, and (d) P 2p of cast and as-deposited alloys after exposure in BBBS for 4 hrs.

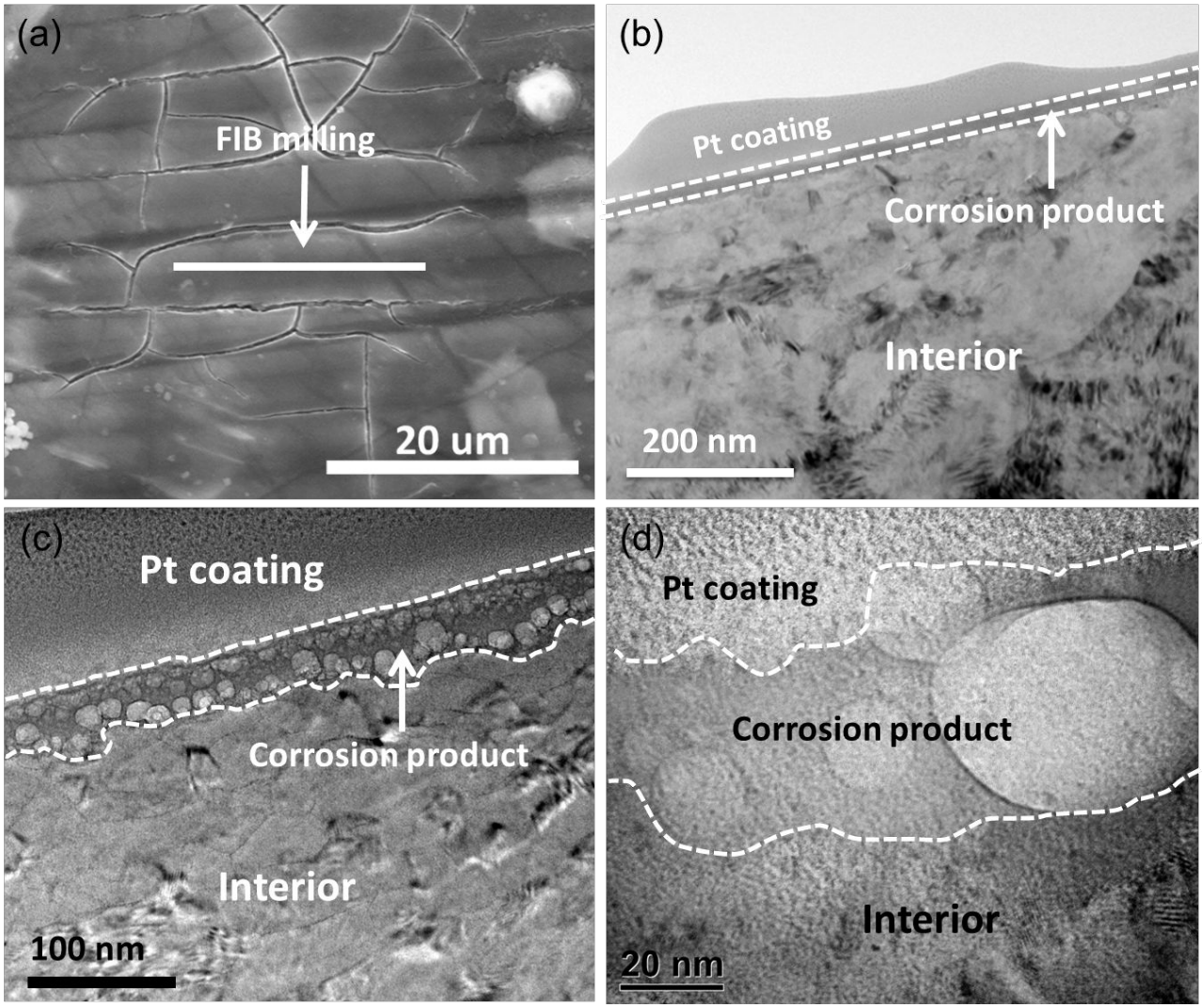

Figure 11. (a) SEM micrographs indicating the location of FIB milling, (b-d) TEM images at different magnifications of cast WE43 alloy after exposure for 90 min in BBBS.

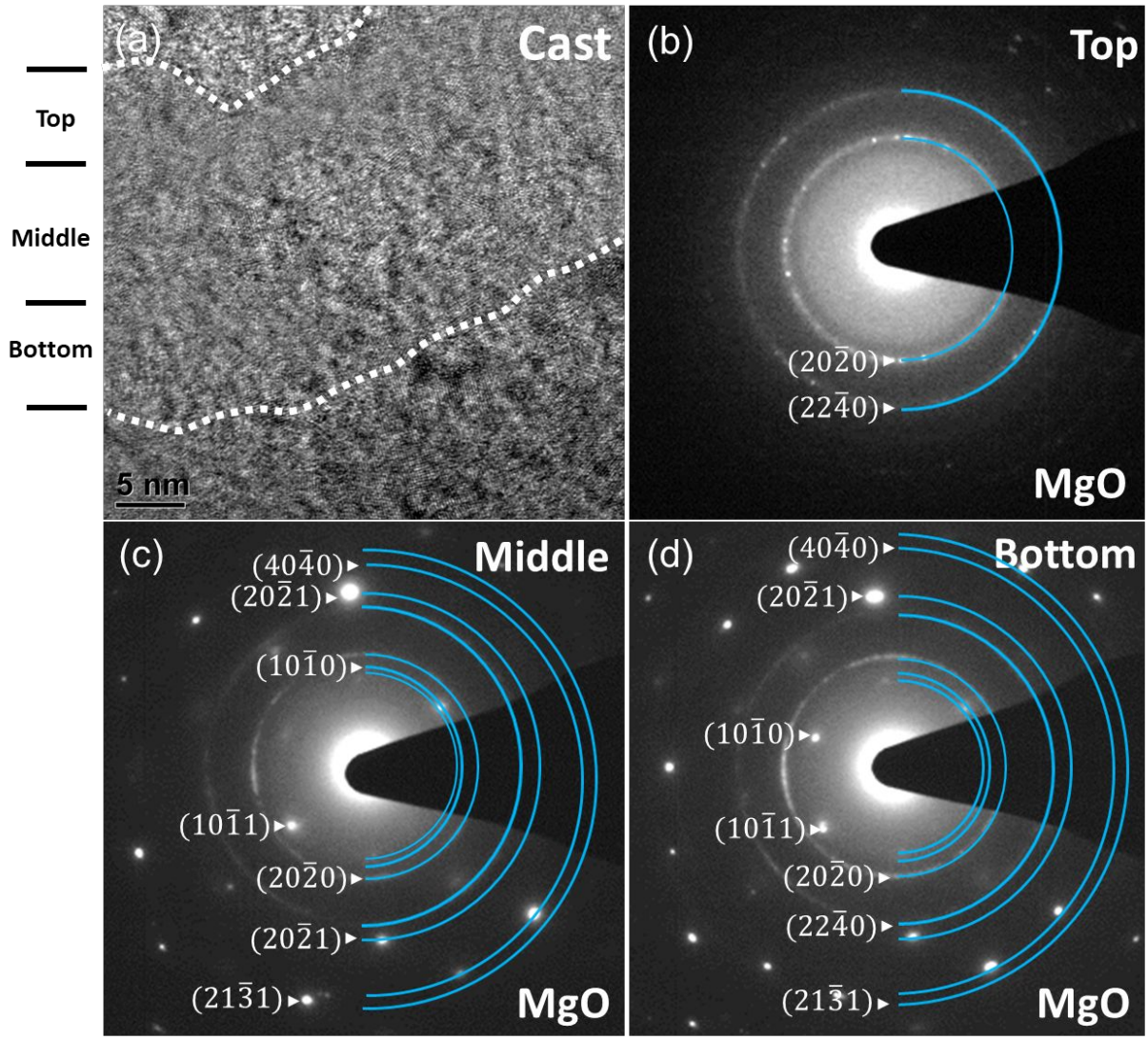

Figure 12. (a) High resolution TEM image and (b-d) SAD of as cast alloy after exposure for 90 min in BBBS.

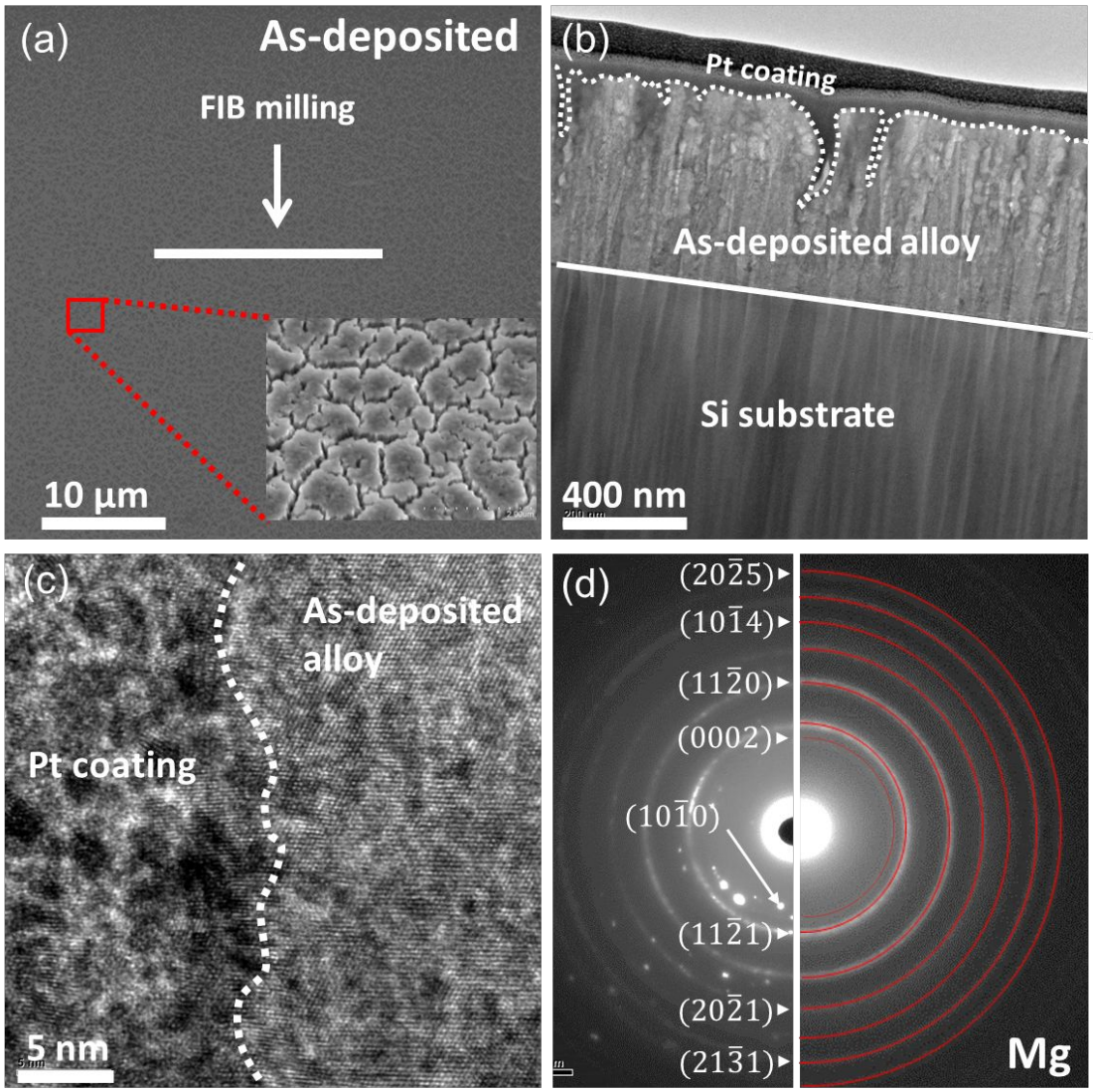

Figure 13. (a) Surface SEM image of a corroded as-deposited sample, (b-c) TEM images and (d) SAD of the topmost surface layer of the sample after exposure for 90 min in BBBS. Inset in (a) shows a magnified SEM image of the corroded surface from the box area. Dashed lines in (b) and (c) represent the sample surface.

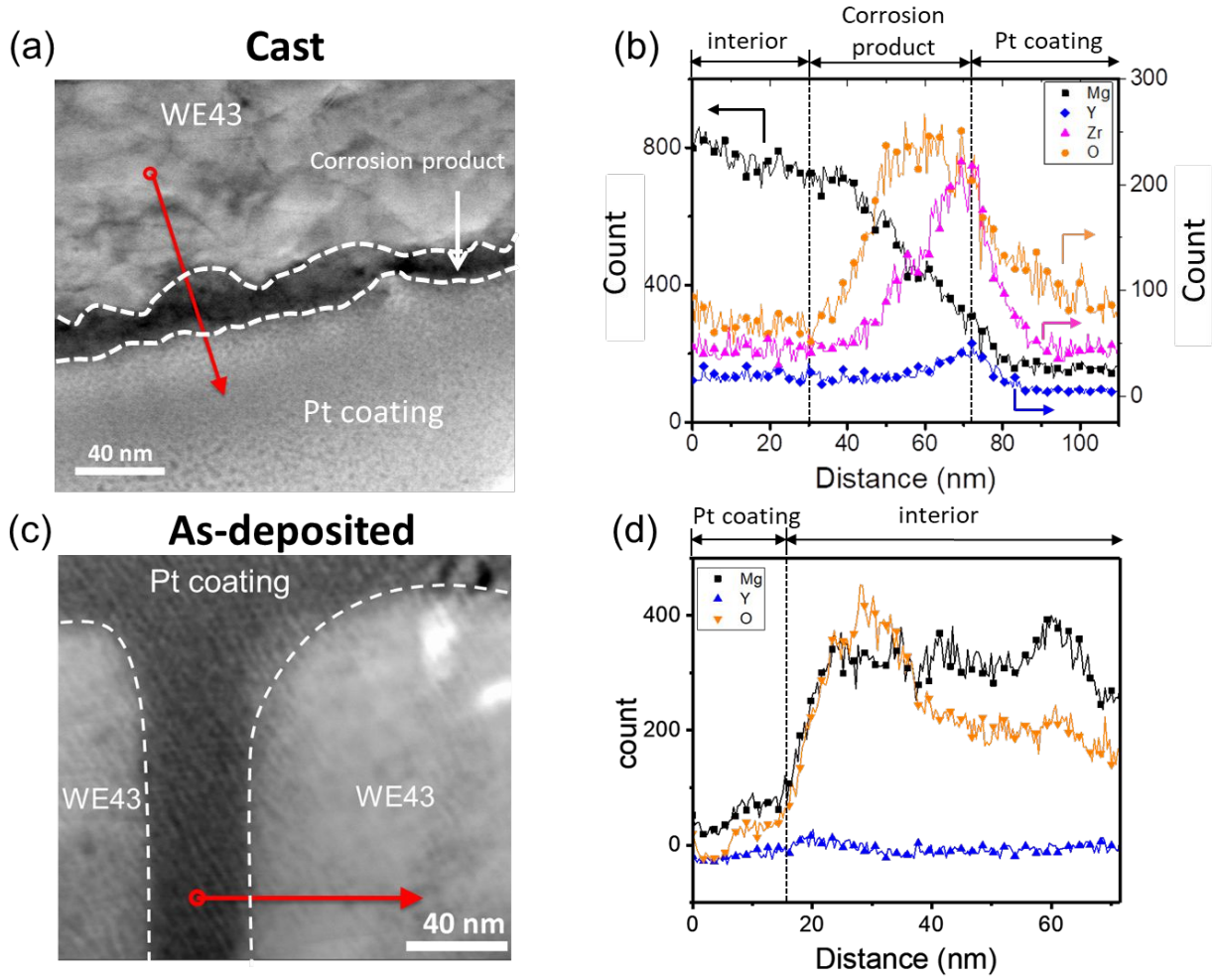

Figure 14. (a and c) STEM image and (b and d) EDS line scan of the corrosion product after exposure for 90 min in BBBS for cast and as-deposited alloys, respectively. In Images (a) and (c), the circle along the arrow represents the start (origin) of the EDS line scan.

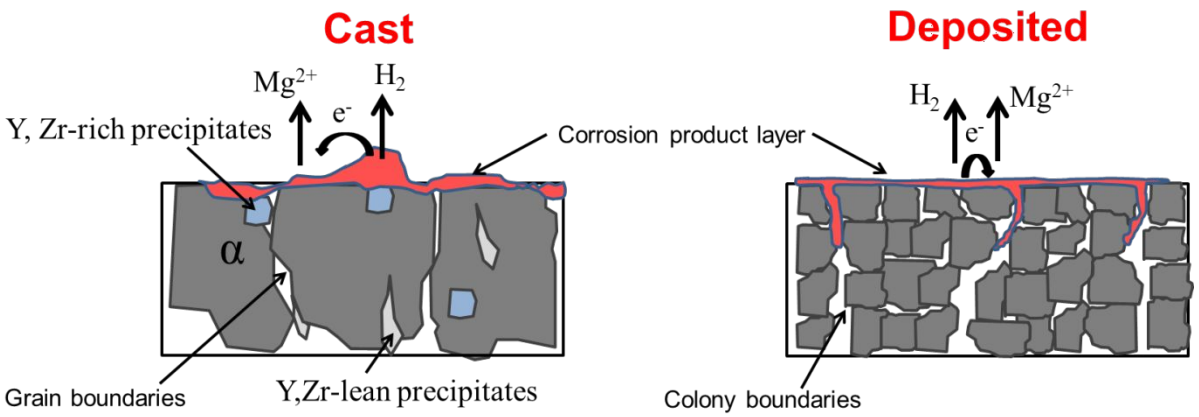

Fig 15. Schematic summary of corrosion process of cast and deposited WE43 Mg alloy in simulated body fluid.